Nano Research

Open Access

Research Article

Inactivated and attenuated meningitis bacteria intracellularly loaded with nanoagents cross blood-brain barrier for glioblastoma immunotherapy

Chen Ji[1,§], Yanping Jiang[1,§], Haoyuan Xu[1], Bin Song[1], Binbin Chu[1] ✉, Yao He[1,2,3] ✉, and Houyu Wang[1] ✉

[1] *Suzhou Key Laboratory of Nanotechnology and Biomedicine, Institute of Functional Nano and Soft Materials (FUNSOM) and Collaborative Innovation Center of Suzhou Nano Science and Technology, Soochow University, Suzhou 215123, China*
[2] *Macao Translational Medicine Center, Macau University of Science and Technology, Taipa 999078, Macau, China*
[3] *Macao Institute of Materials Science and Engineering, Macau University of Science and Technology, Taipa 999078, Macau, China*
[§] *Chen Ji and Yanping Jiang contributed equally to this work.*

Cite this article: *Nano Research*, **2025**, *18*, 94907077. https://doi.org/10.26599/NR.2025.94907077

ABSTRACT: Glioblastoma (GBM) treatment faces a significant challenge due to the blood-brain barrier (BBB) restricting therapeutic delivery. In this study, we found that inactivated and attenuated meningitis bacteria (e.g., *Escherichia coli* K1) intracellularly loaded with nanoagents could safely and effectively bypass the BBB even when injected intravenously into mice at a dose of ~ 10^7 colony forming units (CFU) since the vehicles preserved the bacteria's structure and chemotaxis while removing their pathogenicity. We demonstrated that bacteria could internalize glucose polymer, indocyanine green and stimulator of interferon genes (STING) agonists (e.g., SR717)-modified silica nanoparticles through the bacteria-specific adenosine-triphosphate (ATP)-binding cassette sugar transporter pathway. As a result, the developed system could deliver approximately five times more nanoagents to the brain than free nanoagents. Upon 808-nm irradiation, the indocyanine green induced photothermal effects that destroyed the bacteria, releasing the SR717, which triggered adaptive antitumor immunity, and the bacterial remnants further induced innate antitumor immunity. Our findings demonstrate that this inactivated nanobacteria system effectively treats GBM in mice, suggesting potential for broader applications in central nervous system disorders.

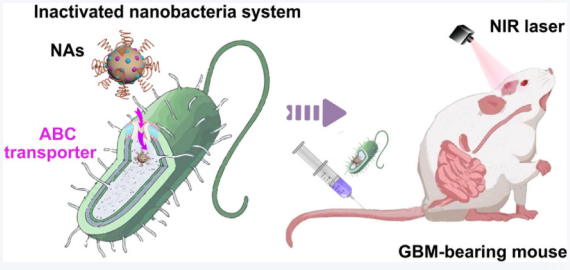

KEYWORDS: bacteria, drug delivery, blood-brain barrier, glioblastoma, immunotherapy

1 Introduction

Glioblastoma (GBM), the most common and aggressive grade IV primary brain tumor in adults, accounted for a significant portion of the 329,673 newly diagnosed cases of central nervous system (CNS) cancer reported worldwide in 2016 by the Global Burden of Disease (GBD) study, corresponding to an age-standardized incidence rate of 4.63 per 100,000 person-years [1–3]. Current treatments, such as surgery combined with chemotherapy (e.g., temozolomide, bevacizumab) and/or radiotherapy, result in a poor 5-year survival rate of less than 10%. While cancer immunotherapy has advanced treatment for metastatic cancers, GBM remains an immunologically "cold" tumor, displaying low levels of proinflammatory immune cells and high levels of immunosuppressive cells within the tumor microenvironment (TME) [4–7]. Recent studies show that activating the stimulator of interferon genes (STING) pathway can convert cold tumors into hot tumors, thereby enhancing antitumor immunity [8–20]. In this pathway, cyclic GMP-AMP synthetase (cGAS) detects cytosolic DNA and catalyzes the formation of 2', 3' cyclic guanosine monophosphate-adenosine monophosphate (cGAMP). cGAMP binds to STING, inducing the production of type I interferons (IFNs) and other cytokines. This cascade activates dendritic cells (DCs) and tumor antigen-specific T cells, and natural killer (NK) cells infiltrate tumors to initiate antitumor responses via STING activation in tumor cells. Consequently, STING agonists such as cGAMP and cyclic dinucleotides (CDNs) have been developed to enhance antitumor immunity [21–25]. However, the poor ability of STING agonists to cross the blood-brain barrier (BBB) poses a significant challenge, leading to off-target inflammation and rapid systemic clearance.

Received: June 22, 2024; **Revised:** September 8, 2024
Accepted: October 17, 2024

✉Address correspondence to Binbin Chu, bbchu@suda.edu.cn; Yao He, yaohe@suda.edu.cn; Houyu Wang, houyuwang@suda.edu.cn

Bacterial therapy, due to bacteria's inherent tumor-targeting abilities, has been explored for cancer treatment [26–36]. The first generation, such as Bacillus Calmette-Guérin (BCG) for bladder cancer, received Food and Drug Administration (FDA) approval in 1990. The second generation involves genetically engineered bacteria with enhanced antitumor activity and improved safety, such as attenuated *Salmonella spp*. lacking lipopolysaccharide (LPS) virulence factors [15]. However, the inability of nonpathogenic bacteria to cross the BBB remains a barrier for GBM treatment [37]. *Escherichia coli* K1 (EC-K1) is a leading cause of neonatal meningitis, capable of crossing the blood-brain barrier (BBB) and triggering severe brain inflammation. Outer membrane protein A (OmpA) plays a crucial role by binding to glycoprotein 96 (gp96) on brain microvascular endothelial cells (BMECs), facilitating EC-K1's tight attachment to the BBB and promoting bacterial invasion. This process involves OmpA-gp96 binding, actin cytoskeleton rearrangement, and activation of signaling pathways like focal adhesion kinase (FAK), phosphatidylinositol 3-kinase (PI3-K), and Rho GTPases, enabling EC-K1 to internalize, evade lysosomal fusion, and cross the BBB [38–41]. Using these bacteria to transport STING agonists across the BBB is a promising but undeveloped approach. Advances in nanotechnology have led to third-generation bacterial therapies, modifying bacterial surfaces with nanomaterials for multifunctional, biorobot-like behaviors [30–36, 42–49]. However, these systems face challenges, including premature drug release, lower payloads, non-specific protein interactions, and potential negative effects on bacterial function or viability. In addition, the pathogenicity of meningitis bacteria used as drug carriers raises safety concerns and limits the deliverable drug dose.

To address these challenges, we designed a novel safe bacterial drug delivery system, in which the nanoagents cargoes were located intracellularly rather than on the surface of inactivated attenuated meningitis bacteria. Typically, we synthesized nanoagents (NAs) composed of (1-4)-glucosidically linked glucose polymer (GP), indocyanine green (ICG), and SR717, incorporated into silica nanoparticles (SiNPs). These nanoagents were internalized by attenuated EC-K1 bacteria via the ATP-binding cassette (ABC) sugar transporter pathway, forming a nanobacteria system that was subsequently inactivated. After intravenous administration to mice, the inactivated nanobacteria system successfully transported SR717 across the BBB, achieving a brain concentration approximately 5.0-fold higher than free nanoagents under similar conditions. Notably, the delivered dose of inactivated bacteria reached ~ 10^7 colony forming units (CFU). Our results demonstrated that inactivated nanobacteria system enabled effective GBM immunotherapy in mice. We anticipate that this inactivated nanobacteria system will inspire innovative therapies for various central nervous system disorders, with the GBM treatment in this study serving as a preliminary proof-of-principle.

2 Experimental

2.1 Synthesis of nanoagents

SiNPs were synthesized by combining 1,8-naphthalimide with 3-aminopropyltrimethoxysilane, followed by exposure to 365-nm ultraviolet (UV) light for 40 min at room temperature. The resulting solution was centrifuged at 6000 rpm for 10 min to remove unreacted chemicals, followed by dialysis (MWCO 1000, Spectra/Pro) for further purification. The purified SiNPs (200 μL, 25 mg/mL) were mixed with GP (100 μL, 10 mg/mL) and incubated at 70 °C for 6 h, after which 0.01 mg of $NaBH_4$ was added. Stable GP-modified SiNPs formed after a 12-h incubation at room temperature. The reaction mixture was filtered using a Nanosep centrifugal device (MW cutoff 3 kDa; Millipore) at 7500 rpm for 15 min to remove unreacted GP. SiNPs with GP molecules (GP-SiNPs) were then combined with SR717 and ICG, and the mixture was shaken overnight at 4 °C. Unreacted ICG was removed by centrifugation at 8000 rpm for 10 min using Nanosep centrifugal devices (MW cutoff 3 kDa; Millipore). The resulting NAs were collected and stored at 4 °C for subsequent studies. To determine the size and shape of the NAs, we used transmission electron microscopy (TEM, Philips CM 200) operating at 200 kV. We measured the ultraviolet–visible (UV–vis) absorption spectra using a UV–vis near-infrared spectrophotometer (Perkin-Elmer lambda 750) and recorded the photoluminescence (PL) spectra using a spectrofluorimeter (HORIBA JOBIN YVON FLUORMAX-4). Dynamic light scattering (DLS) analysis was conducted using a Beckman Coulter, Inc., DelsaTM nano submicron particle size analyzer.

2.2 Bacterial culture

The EC-K1 strains were obtained from the American Type Culture Collection (ATCC). The bacteria were grown in Luria-Bertani (LB) liquid media at 250 rpm and 37 °C and harvested during the exponential growth phase. Bacterial suspensions were washed three times with PBS, and the optical density (OD) at 600 nm was measured to determine the bacterial concentration. The number of bacterial colonies was counted using a colony counting device (Czone 8).

2.3 Construction of attenuated bacteria

We cultivated EC-K1 cells in 50 mL of LB liquid medium until the OD reached approximately 0.8, then centrifuged to collect the cells. The cells were resuspended in 2 mL of 10% glycerol after three washes with 10% glycerol. The *msbB* sgRNA plasmid and homologous repair arm of *msbB* were added to the competent cells and left on ice for five minutes. After electroporation at 2500 V, 1 mL of LB medium was added. Following a one-hour recovery phase at 37 °C, the cells were plated on spectinomycin or kanamycin-resistant plates to select *msbB* deletion strains.

2.4 Construction of inactivated nanobacteria system

ΔBac (+) suspension containing approximately 1.0×10^7 CFU was incubated with NAs (0.56 mM, 200 μL) in a shaking incubator at 200 rpm and 37 °C for 4 h. The mixture was centrifuged at 6000 rpm for 5 min to harvest NAs-ΔBac (+). The harvested cells were washed at least three times with PBS to remove excess or nonspecifically absorbed NAs. One milliliter of NAs-ΔBac (+) was added to a 60 mm-diameter culture dish and exposed to UV irradiation using a 16 W UV lamp at 254 nm while being shaken on a magnetic stirrer for 120 min, producing NAs-ΔBac (−).

2.5 Cellular experiments

Mouse glioblastoma cell lines bEnd.3, GL261, and GL261-luc were obtained from Shanghai Zhong Qiao Xin Zhou Biotechnology and cultured under appropriate conditions. Bone marrow cells from female C57BL/6J mice were washed with red blood cell (RBC) lysis buffer (Sigma) and subjected to hypotonic lysis to reduce RBC content. After three days of growth at a starting concentration of

1×10^6 cells/mL in RPMI 1640, nonadherent cells were washed away. On day 6, an additional 10 mL of fresh complete medium containing 20 ng/mL rmGM-CSF (MCE) was added, and half of the medium was replaced. On day 8, nonadherent and loosely adherent cells were collected by forceful pipetting and placed in the lower chamber of the transwell system. GL261 cells were inoculated in a 96-well plate, co-incubated for 6 h with NAs, NAs-ΔBac (–) without SR717, or NAs-ΔBac (–), exposed for 5 min with or without an 808-nm laser, and then washed with sterile PBS. Cell viability was assessed using the 3-(4,5)-dimethylthiahiazo (-z-y1)-3,5-di-phenytetrazoliumromide (MTT) assay. Treated cells were also subjected to confocal microscopy analysis after staining with calcein-AM (CAM) and propidium iodide (PI) (λ_{ex} = 488 nm, λ_{em} = 500–545 nm for CAM, λ_{ex} = 543 nm, λ_{em} = 560–620 nm for PI).

2.6 Mouse brain microvascular endothelial cell model

An *in vitro* mouse brain microvascular endothelial cell (bEnd.3) model was created using a 24-well transwell plate with a 0.4 μm pore size membrane. Transwell inserts 6.5 mm in diameter were seeded with bEnd.3 cells at 1.0×10^4 cells per well. A Millicell-ERS volt-ohmmeter was used to measure the transendothelial electrical resistance (TEER) to maintain the integrity of the cell monolayer during culture.

2.7 Animal experiments

All animal experiments involved in this study were conducted in accordance with relevant laws and protocols approved by the Animal Care and Use Committee of Soochow University (Approval No. ECSU-2019000198). GBM-bearing mouse models were established using a brain stereotaxic apparatus to locate and inject GL261-luc cells into the mouse brain. Tumor size was measured using biofluorescence signals, with the tumor volume not exceeding a maximum diameter of 15 mm. To investigate *in vivo* bacterial dispersion, healthy mice were intravenously injected with mCherry@ΔBac, mCherry@*E. coli* DH5α, NAs-ΔBac (+), or NAs-ΔBac (–) (~ 1.0×10^7 CFU per mouse). Mice were sacrificed at intervals (12, 24, 72, and 120 h), and the brain, heart, liver, spleen, lung, and kidney were harvested for imaging using an *in vivo* optical imaging system (IVIS Lumina III). Homogenized organs were centrifuged, and bacterial colonies were counted using a colony counting instrument (Czone 8). To examine therapeutic effects *in vivo*, GBM-bearing mice were injected with PBS, NAs, NAs-ΔBac (–) without SR717, or NAs-ΔBac (–) (~ 1×10^7 CFU of ΔBac internalized with NAs (0.56 mM)). Seven days post-inoculation, an 808-nm laser (1.2 W/cm^2) was used to irradiate the GBM for 5 min, keeping the temperature constant at 48 °C. The mice received additional injections and laser exposure at 5 and 10 days post-initial injection. Bioluminescence imaging was performed every four days to assess antitumor effects. Two days after the final treatment, mouse brain tissues were homogenized into single-cell suspensions for flow cytometry analysis. Detailed information about the antibody panel used is provided in Table S1 in the Electronic Supplementary Material (ESM).

2.8 Statistical analysis

We processed confocal images using ImageJ (NIH Image; http://rsbweb.nih.gov/ij/) and Leica Application Suite Advanced Fluorescence Lite (LAS AF Lite). Error bars represent the standard deviation from three independent measurements. All statistical analyses were performed using GraphPad Prism 7 and Origin. Statistical significance was determined using one-way ANOVA.

3 Results and discussion

3.1 General design of the inactivated nanobacteria system

We developed a bacterial drug delivery system utilizing intracellularly loaded NAs, composed of four key components: SiNPs, SR717, GP, and ICG, as illustrated in Fig. 1(a). Using Schiff base interactions between amino groups on the SiNP surface and aldehyde groups of GP molecules, we successfully modified the SiNP with GP molecules [50–53]. Subsequently, we loaded the SiNPs with ICG and SR717 molecules through electrostatic interactions, forming the complete NAs. Compared to cGAMP, SR717 is more stable, has better pharmacokinetic properties, and is easier and less costly to synthesize. This makes it more effective and practical for therapeutic use [54]. The core of the NAs, SiNPs are under clinical evaluation for various biomedical applications due to their demonstrated safety, efficacy, and viability [55, 56]. GP molecules (e.g., poly[4-O-(α-D-glucopyranosyl)-D-glucopyranose]) serve as unique carbon sources for bacteria and are robustly engulfed by bacterial cells, not mammalian cells, via a bacteria-specific ABC sugar transporter pathway [57–59]. This mechanism enabled bacteria to uptake the GP-modified nanoparticles. Similarly, attenuated meningitis bacteria (e.g., EC-K1) consumed these camouflaged "foods" in the form of nanoagents (Fig. 1(b)).

We attenuated EC-K1 by knocking out the *msbB* gene, which removed the myristoylation of lipid A (a potent endotoxin), thereby eliminating the toxicity of LPS. Polymerase chain reaction (PCR) (Fig. S1 in the ESM) and Sanger sequencing (Table S2 in the ESM) confirmed the successful construction of attenuated EC-K1 (ΔBac (+)). To further mitigate potential toxicity from host bacterial proliferation, we inactivated them by using UV irradiation after the internalization of nanoagents (NAs-ΔBac (–)) (Fig. 1(c)). UV irradiation preserves the bacterial structure and outer membrane protein activity better than other inactivation methods (e.g., heat, ethanol). The OmpA protein on the outer membrane of EC-K1 binds to the gp96 protein on BMECs, triggering actin cytoskeleton rearrangement that allows EC-K1 to invade the brain [60–62]. Therefore, the constructed NAs-ΔBac (–) strain retained the ability of live EC-K1 to cross the BBB while losing its pathogenicity from LPS and its proliferative capacity (Fig. 1(d)).

Near-infrared (NIR) irradiation (e.g., 808 nm) was used to destroy NAs-ΔBac (–), releasing the intracellularly loaded SR717 due to the heat generated by the ICG molecules. When SR717 binds to STING, it triggers the production of IFNs and other cytokines [14, 15]. This stimulation specifically activates antigen-presenting cells, particularly DCs, which in turn prime and activate tumor antigen-specific T lymphocytes. Furthermore, the activation of the STING pathway in tumor cells may allow NK cells to infiltrate the tumor and initiate an anticancer response (Fig. 1(e)). Additionally, the destruction of bacterial cells can induce innate antitumor immunity. Pathogen-associated molecular patterns (PAMPs) generated by bacterial debris activate innate immune cells, including macrophages and NK cells. Ultimately, both adaptive and innate antitumor immunity induced by this bacteria-based drug delivery system could provide effective therapeutic outcomes for GBM.

3.2 Preparation and characterization of the inactivated nanobacteria system

We first systematically prepared and characterized the nanoagents. As schematically illustrated in Fig. S2 in the ESM, we modified GP-

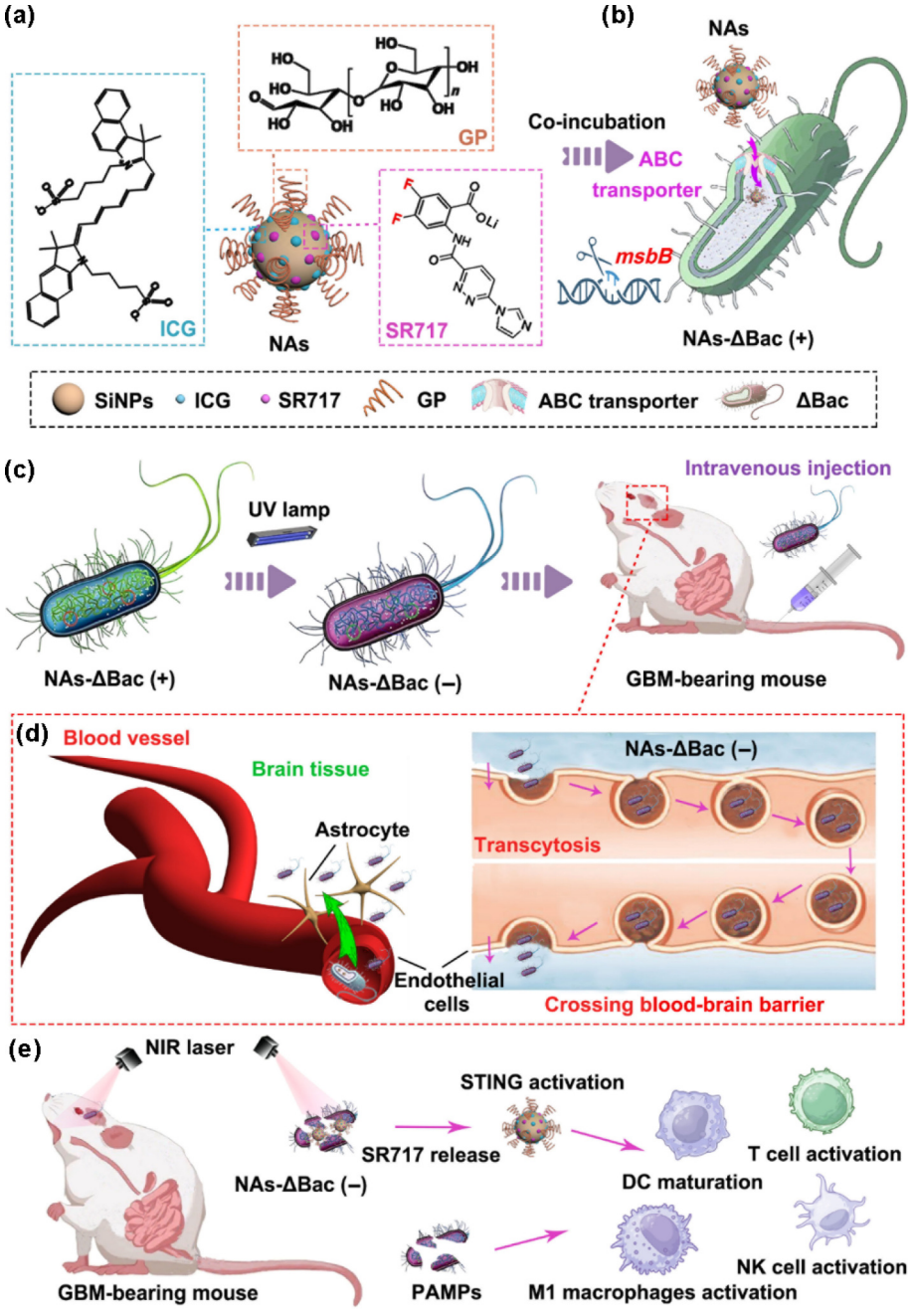

Figure 1 Design of the inactivated nanobacteria system. (a) A scheme illustrating the main composition of NAs, including SiNPs, GP, ICG, and SR717. (b) A scheme illustrating the internalization of NAs into attenuated EC-K1 (NAs-ΔBac (+)) through a bacteria-specific ABC sugar transporter. (c) A scheme illustrating the inactivation of NAs-ΔBac (+) via UV irradiation (NAs-ΔBac (–)), followed by intravenous injection into GBM-bearing mice. (d) A scheme illustrating that NAs-ΔBac (–) can safely circumvent the BBB. (e) A scheme illustrating the controllable release of SR717 from host bacterial cells under NIR laser irradiation, triggering adaptive antitumor immunity and innate antitumor immunity.

SiNPs based on previously reported methods [50–53]. We then loaded the SiNPs with ICG and SR717 molecules via electrostatic interactions, forming the nanoagents. We characterized the nanoagents using TEM, DLS, zeta potential measurements, UV-vis, and PL measurements. The TEM images (Fig. S3(a) in the ESM) showed that the as-prepared nanoagents appeared as highly dispersed spherical particles with an average diameter of ~ 5 nm, slightly larger than that of the naked SiNPs (~ 3 nm). The size distribution determined by DLS was consistent with these results (Fig. S3(b) in the ESM). Zeta potential measurements (Fig. S3(c) in the ESM) indicated that GP-SiNPs were positively charged, while ICG and SR717 were negatively charged, confirming their adsorption via electrostatic interactions. The UV spectra of the nanoagents displayed representative peaks for SR717 (300 nm) and ICG (731, 780 nm) (Fig. S3(d) in the ESM). Calibration absorption curves quantified the amounts of SR717 and ICG modified onto the SiNPs (Figs. S3(e) and S3(f) in the ESM). PL spectra showed the emission peaks of SR717 and ICG in the nanoagents (Figs. S3(g) and S3(h) in the ESM). Additionally, the nanoagents demonstrated good stability under various conditions (Fig. S4 in the ESM),

supporting their potential biomedical applications. These results confirmed the successful preparation of nanoagents.

Next, we constructed attenuated bacteria intracellularly loaded with nanoagents (NAs-ΔBac (+)). We incubated an attenuated *E. coli* K1 strain (ΔBac (+)) (~ 10^7 CFU, 1 mL) with the constructed nanoagents (0.56 mM) at 37 °C, rinsing away any unincorporated NAs with PBS. To obtain inactivated bacteria intracellularly loaded with nanoagents (NAs-ΔBac (−)), we irradiated NAs-ΔBac (+) (~ 10^7 CFU, 1 mL) with an ultraviolet lamp (16 W/cm^2, 2 h). Scanning electron microscopy (SEM) images (Fig. 2(a)) showed that the surface and morphology of NAs-ΔBac (+/−) were similar to those of natural bacteria. High-angle annular dark field-scanning transmission electron microscopy (HAADF-STEM) images (Fig. 2(b)) revealed the elemental mapping of NAs-ΔBac (+/−), showing the presence of silicon from SiNPs and fluorine from SR717 only in NAs-ΔBac (+/−), not in the live attenuated *E. coli* K1 (ΔBac (+)). Confocal laser scanning microscopy (CLSM) images (Fig. 2(c)) showed both green fluorescence signals from SR717 (λ_{ex} = 405 nm, λ_{em} = 500–550 nm) and red fluorescence signals from ICG (λ_{ex} = 633 nm, λ_{em} = 700–800 nm) in NAs-ΔBac (+/−) but not in ΔBac (+/−). No fluorescence was observed in the ΔBac (+) strain incubated with nanoagents without GP modification (Fig. S5 in the ESM). We created two *E. coli* mutants, ΔmalE and ΔlamB, with aberrant expression of the bacteria-specific ABC sugar transporter

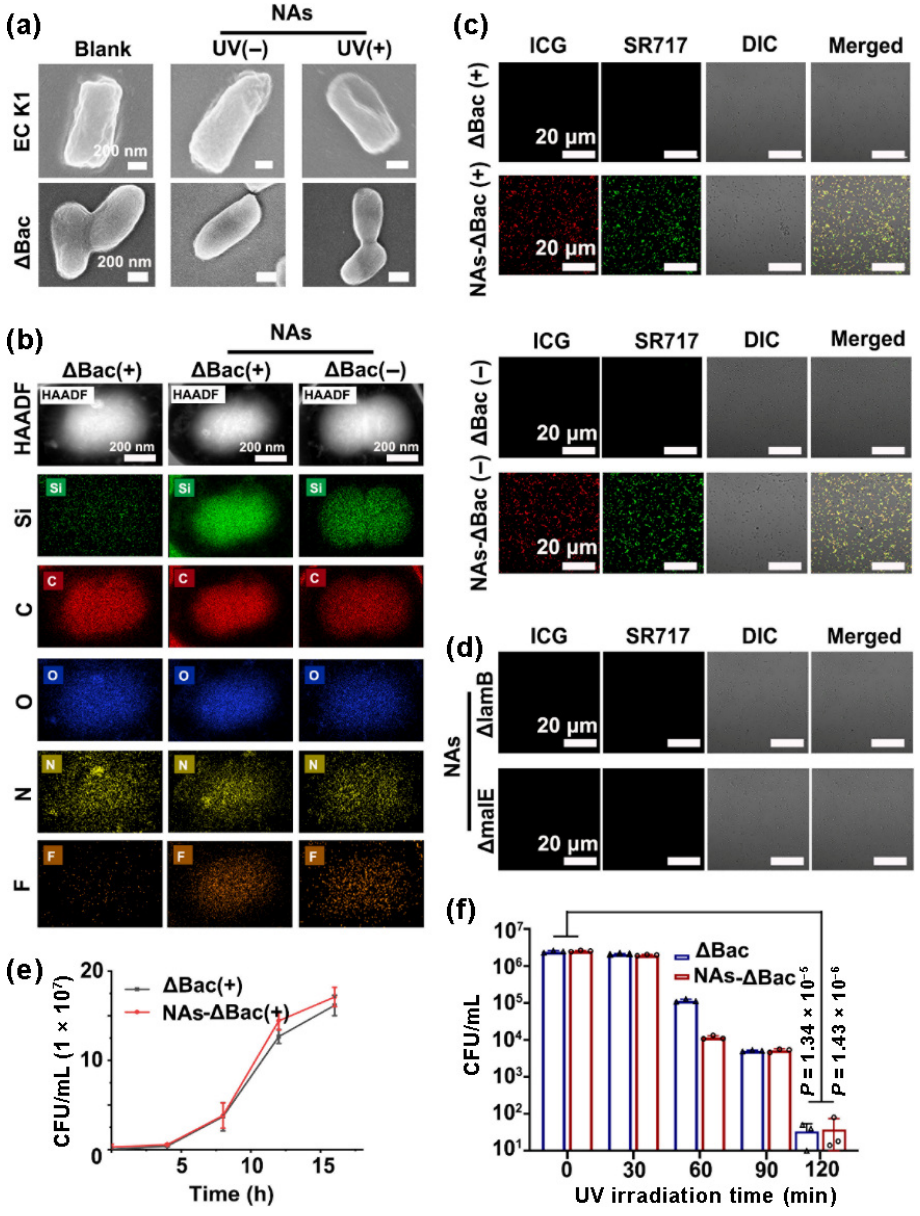

Figure 2 Characterization of the inactivated nanobacteria system. (a) SEM images of EC-K1 (Bac (+)), attenuated EC-K1 (ΔBac (+)), NAs-Bac (+), NAs-ΔBac (+), NAs-Bac (−) and NAs-ΔBac (−). Scale bars: 200 nm. (b) HAADF-STEM images of attenuated EC-K1 (ΔBac (+)) treated with PBS or NAs with or without UV irradiation. The bacterial cell concentration was ~ 1.0 × 10^7 CFU. Scale bars: 200 nm. (c) CLSM images of ΔBac (+), NAs-ΔBac (+), ΔBac (−) and NAs-ΔBac (−). Scale bars: 20 μm. (d) CLSM images of bacterial mutants of ΔlamB and ΔmalE incubated with NAs. Scale bars: 20 μm. (e) Proliferation plots of ΔBac (+) or NAs-ΔBac (+). (f) The viability of ΔBac or NAs-ΔBac upon UV irradiation for different durations was tested by agar plate experiments. All imaging tests were performed three times, each yielding consistent outcomes. The standard deviation derived from three separate measurements is represented by the error bars. The statistical significance of differences was determined using a Tukey post hoc test and one-way analysis of variance (ANOVA).

(Tables S3 and S4 in the ESM). Fluorescent signals were absent in the nanoagents-treated mutants (Fig. 2(d)), consistent with flow cytometry data (Fig. S6 in the ESM). Inhibition and competition assays (Fig. S7 in the ESM) confirmed that the bacteria-specific ABC sugar transporter pathway facilitated nanoagents entry into the bacteria. The internalization of nanoagents did not influence the proliferation of host bacteria (Fig. 2(e)). Flow cytometry (Fig. S8 in the ESM) evaluated the nanoagents loading efficiency of ΔBac (+) after a 4-h incubation, showing that concentrations greater than 0.56 mM did not significantly improve the drug loading efficiency (~ 60.2%). Thus, we used 0.56 mM nanoagents for subsequent tests. Liquid medium turbidity assays (Fig. S9 in the ESM) and agar plate studies (Fig. 2(f)) assessed the survivability of ΔBac and NAs-ΔBac upon UV irradiation. After 120 min of UV irradiation, bacterial counts of ΔBac and NAs-ΔBac decreased by nearly 99.99%, indicating complete inhibition of bacterial proliferation. These results demonstrated the successful construction of the inactivated nanobacteria system.

3.3 Inactivated nanobacteria system crossing the BBB *in vitro* and *in vivo*

To determine whether the inactivated nanobacteria system can cross the BBB, we first constructed an *in vitro* BBB model using bEnd.3 cells (Fig. 3(a)). We evaluated this model using the transepithelial electrical resistance (TEER) assay (Fig. S10 in the ESM). Typically, NAs-ΔBac (+/−) systems were cultured with 1.0×10^5 CFU of bEnd.3 cells in the upper transwell compartment. We collected the culture media at 1, 2, 3, and 4 h from the lower transwell chamber. The penetration rate of NAs-ΔBac (−) was 80.5% at 4 h, closely matching the 83.6% penetration rate of NAs-ΔBac (+) (Fig. 3(b)). These findings demonstrated that inactivated nanobacteria system retains the ability of *E. coli* K1 to bypass the BBB *in vitro*.

We further investigated the mechanism by which the inactivated nanobacteria system crosses the BBB. Previous studies have shown that OmpA, a 325 amino acid protein located on the outer membrane of *E. coli* K1, plays a critical role in crossing the BBB. OmpA binds to gp96, a heat shock protein analog found on the surface of BMECs, triggering actin cytoskeleton rearrangement and subsequent bacterial invasion [60–62]. To explore the role of OmpA and gp96 in the crossing of the BBB by NAs-ΔBac (−), we designed competition experiments. We incubated NAs-ΔBac (−) with an OmpA antibody for 1.5 h before cultivating with bEnd.3 cells (Fig. 3(c)). The penetration of NAs-ΔBac (−) was progressively inhibited with increasing concentrations of the OmpA antibody. Similarly, we treated bEnd.3 cells with a gp96 antibody for 1.5 h before introducing NAs-ΔBac (−) (Fig. 3(d)). The penetration rate of NAs-ΔBac (−) decreased with increasing concentrations of the gp96 antibody. These results collectively demonstrate that the inactivated nanobacteria system can effectively bypass the BBB *in vitro*, potentially via the interaction between OmpA and gp96.

Building on our *in vitro* findings, we evaluated whether the inactivated nanobacteria system could cross the BBB *in vivo*. To track the bacteria in mice post-injection, we engineered bacteria to express the red fluorescent protein mCherry by transforming the pRSETB-mCherry plasmids into attenuated *E. coli* K1 (mCherry@ΔBac) or *E. coli* DH5α (mCherry@*E. coli* DH5α) strains (Fig. S11 in the ESM). We then intravenously injected healthy female BALB/c mice with approximately 1×10^7 CFU of mCherry@ΔBac or mCherry@*E. coli* DH5α. The mice were sacrificed 12 h post-injection, and we used an *in vivo* imaging system (IVIS Lumina III) to detect mCherry signals from major organs *ex vivo* (Fig. S12 in the ESM). After 12 h, the red fluorescence of mCherry@ΔBac was prominently observed in the liver, lung, kidney, and brain, while mCherry@*E. coli* DH5α was mainly detected in the liver, lung, and kidney. Quantitatively, the fluorescence intensity of mCherry@ΔBac in the brain was ~ 6.5 times higher than that of mCherry@*E. coli* DH5α. Agar plate assays confirmed that the number of bacteria in the brain of the mCherry@ΔBac group was significantly higher (~ 4.3 times) than in the mCherry@*E. coli* DH5α group (Fig. S13 in the ESM). These results suggest that attenuated *E. coli* K1 accumulates in the brain more effectively than *E. coli* DH5α.

We then examined the ability of the inactivated nanobacteria system to cross the BBB *in vivo* after intravenous injection. Female nude mice were randomized into four groups (n = 3 per group): G1, PBS; G2, NAs; G3, NAs-ΔBac (+); and G4, NAs-ΔBac (−). At 4 h post-injection, we observed strong fluorescence from ICG in the brains of the NAs-ΔBac (+) and NAs-ΔBac (−) groups, with fluorescence intensity peaking at 8 h post-injection (Fig. 3(e)). The *ex vivo* images corroborated the *in vivo* observations (Figs. 3(f) and 3(g)). Quantitatively, the NAs signal in the brain at 8 h in the G4 group (NAs-ΔBac (−)) was ~ 5 times greater than that in the G2 group (pure NAs), indicating effective delivery of STING agents to the brain by the inactivated nanobacteria system. TEM imaging confirmed the accumulation of NAs-ΔBac (+) and NAs-ΔBac (−) in the mouse brain (Fig. 3(h)). Collectively, these results demonstrate that the inactivated nanobacteria system has the potential to cross the BBB *in vivo*.

3.4 Antitumor effects of the inactivated nanobacteria system *in vitro*

To investigate the antitumor effects of the inactivated nanobacteria system *in vitro*, we designed a transwell system. Mouse glioblastoma cells (Gl261) subjected to different treatments (PBS, NAs, ΔBac (−), NAs-ΔBac (−) without SR717 + laser, and NAs-ΔBac (−) + laser) were placed in the upper chamber, while DCs harvested from the bone marrow (BMDCs) of 6- to 8-week-old female C57BL/6 mice were seeded in the lower chamber (Fig. 4(a)). After 300 s of 808-nm laser irradiation (1.2 W/cm^2), the temperature of 1.0×10^7 CFU/mL NAs-ΔBac (−) loaded with 0.56 mM NAs reached ~ 50 °C, similar to the temperature reached by the equivalent NAs alone (Fig. S14 in the ESM). This temperature increase was due to the photothermal effect of ICG molecules in the NAs. SEM images (Fig. 4(b)) showed lysed bacterial cells only in the NAs-ΔBac (−) without SR717 and NAs-ΔBac (−) groups after laser irradiation, suggesting that the elevated temperature destroyed the bacterial cells, possibly releasing the loaded NAs. Additionally, we demonstrated that the photothermal effects of NAs-ΔBac (−) could destroy glioblastoma Gl261 cells (Fig. S15 in the ESM).

We next analyzed the expression levels of phosphorylated STING (p-STING), phosphorylated TBK1 (p-TBK1), and phosphorylated IRF3 (p-IRF3) in Gl261 cells under different treatments (PBS, NAs, ΔBac (−), NAs-ΔBac (−) without SR717+ laser, and NAs-ΔBac (−) + laser) using Western blotting. Phosphorylation of STING, TBK1, and IRF3 was significantly increased in the NAs-ΔBac (−) + laser group (Fig. 4(c)). For the BMDCs in the lower chamber, enzyme-linked immunosorbent assay (ELISA) showed elevated expression of interferon-β (IFN-β)

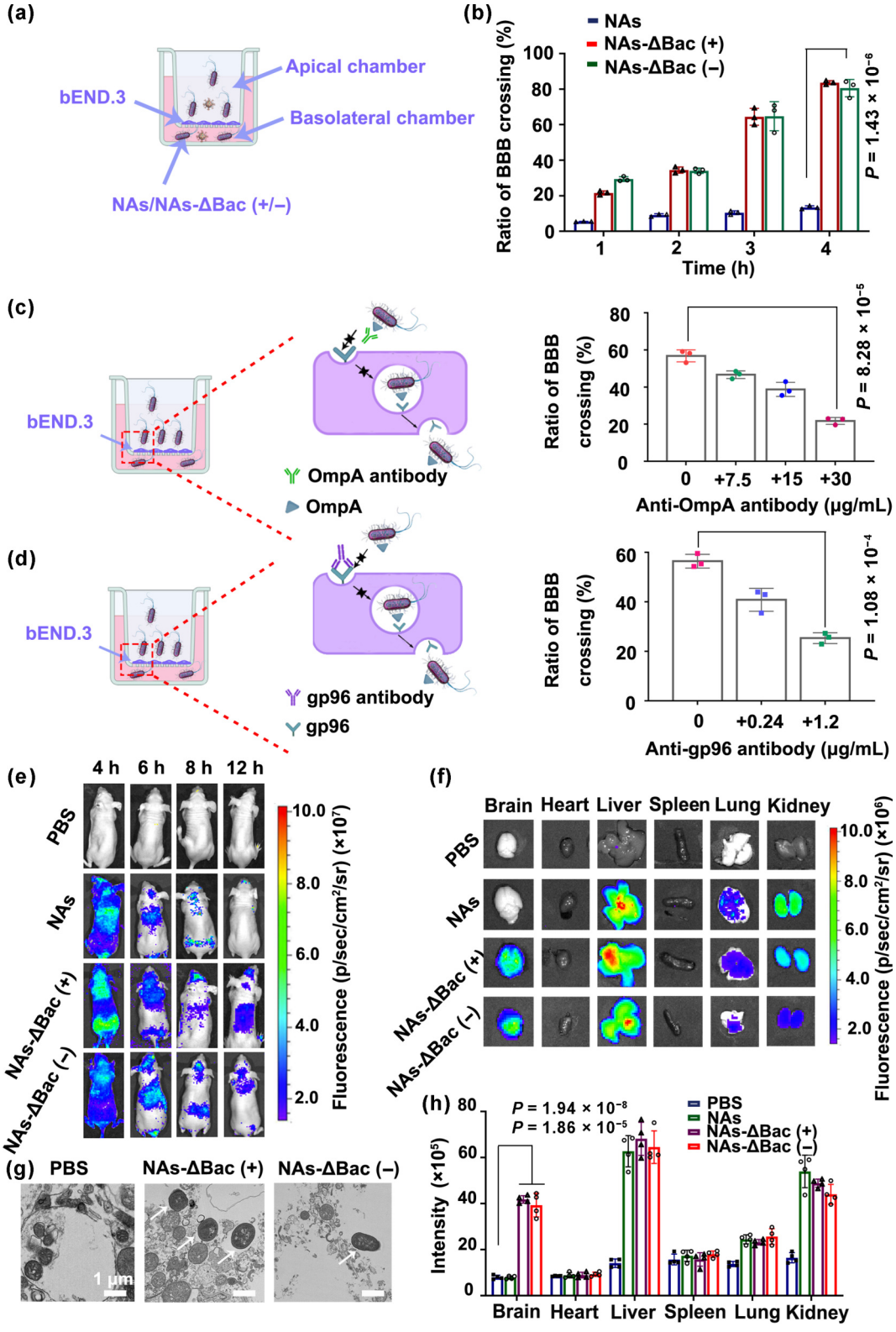

Figure 3 Inactivated nanobacteria system crossing the BBB *in vitro* and *in vivo*. (a) Diagram depicting the construction of the *in vitro* BBB model using bEnd.3 cells. (b) The penetration rates of NAs, NAs-ΔBac (+), and NAs-ΔBac (–) after 1, 2, 3, and 4 h of incubation. The bacterial count was approximately 1.0×10^5 CFU. (c) Scheme displaying competition trials to demonstrate the uptake of NAs-ΔBac (–) by bEnd.3 cells linked with OmpA and the corresponding penetration rates of NAs-ΔBac (–) in the presence of the OmpA antibody. The NAs-ΔBac (–) cells were initially treated with the OmpA antibody for 1.5 h before inoculation with bEnd.3 cells. (d) Scheme displaying competition trials to demonstrate the uptake of NAs-ΔBac (–) by bEnd.3 cells associated with the gp96 antibody and the related penetration rates of NAs-ΔBac (–). (e) Representative *in vivo* fluorescence images of mice intravenously injected with PBS, NAs, NAs-ΔBac (+), or NAs-ΔBac (–) over time. (f) Corresponding *ex vivo* imaging of major organs at 8 h after intravenous injection and (g) the corresponding fluorescence intensity. (h) TEM images of mouse brains following various treatments, as indicated. All imaging experiments were repeated three times with similar results. The error bars represent the standard deviation obtained from three independent measurements. The statistical significance was calculated via one-way analysis of variance (ANOVA) with a Tukey post hoc test.

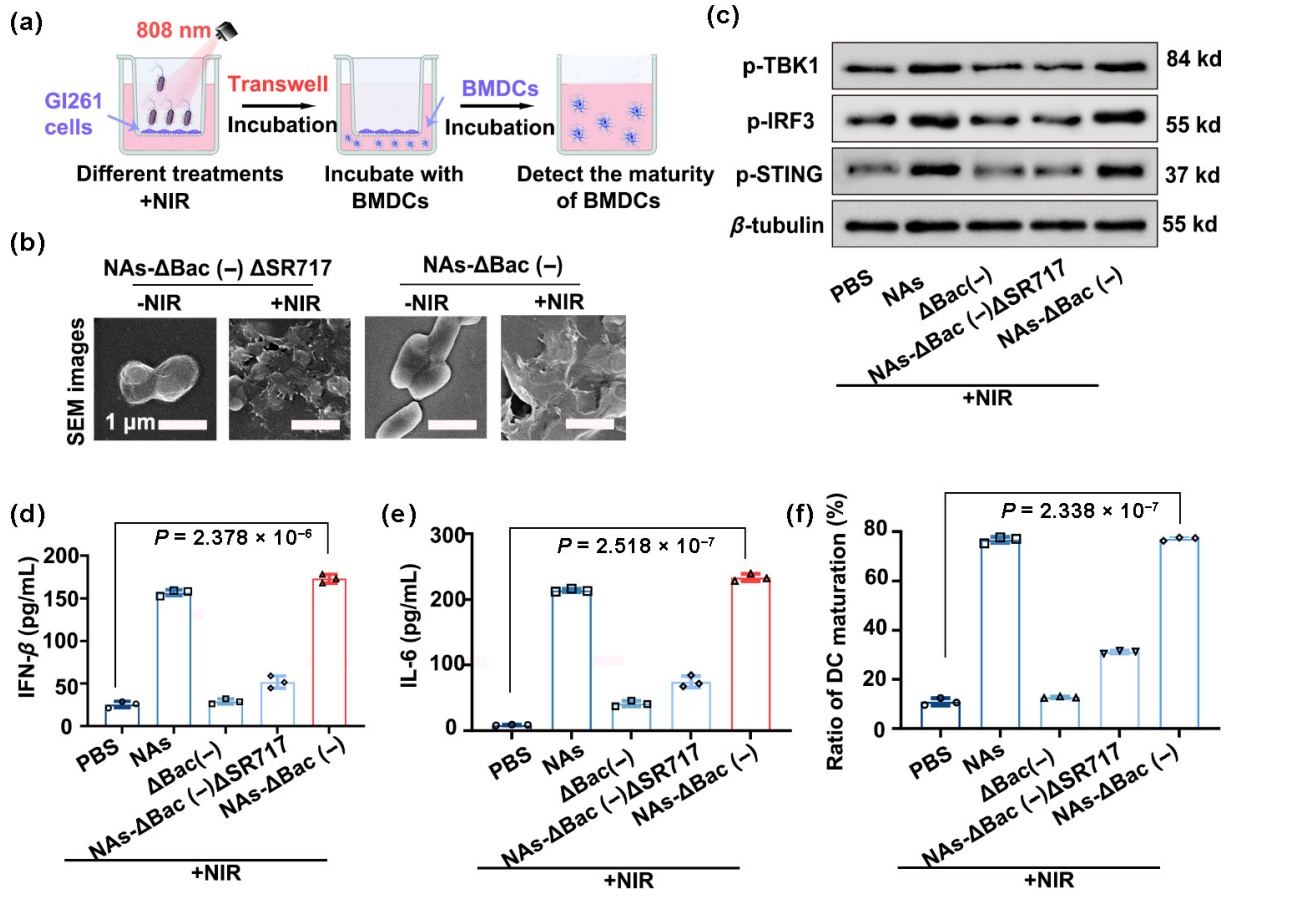

Figure 4 *In vitro* evaluation of the antitumor ability of the inactivated nanobacteria system. (a) A scheme illustrating the Transwell system for investigating the antitumor effects of the constructed NAs-ΔBac (–) system *in vitro*. Gl261 cells were cultured in the upper chamber, and BMDCs were cultured in the lower chamber. (b) SEM images of NAs-ΔBac (–) ΔSR717 (*i.e.*, NAs-ΔBac (–) without SR717) and NAs-ΔBac (–) with or without irradiation. Scale bars: 1 μm. (c) Western blot analysis of p-STING, p-TBK1 and p-IRF3 in Gl261 cells after different treatments, as indicated. The levels of the inflammatory factors (d) IFN-β and (e) IL-6 secreted by BMDCs in the lower chamber after different treatments, as indicated. (f) Flow cytometric analysis of mature BMDCs ($CD11c^+$ MHC II^+) after different treatments as indicated. All imaging experiments were repeated three times with similar results. All error bars represent the standard deviation determined from three independent assays. The statistical significance was calculated via one-way analysis of variance (ANOVA) with a Tukey post hoc test.

(Fig. 4(d)) and interleukin-6 (IL-6) (Fig. 4(e)) in the NAs + laser and NAs-ΔBac (–) + laser groups. Flow cytometry was used to evaluate the maturation of BMDCs ($CD11c^+$ and MHC II^+ cells). Detailed information about the antibody panel used for spectral flow cytometry analyses is provided in Table S1 in the ESM. The highest level of BMDC maturation was observed in the NAs-ΔBac (–) + laser group (Fig. 4(f) and Fig. S16 in the ESM). Collectively, these results indicate that the inactivated nanobacteria system, after NIR irradiation, can effectively stimulate the cGAS-STING pathway *in vitro*.

3.5 Biosafety assessment of the inactivated nanobacteria system

We thoroughly examined the biosafety of the inactivated nanobacteria system following intravenous injection in healthy mice (Fig. 5(a)). Initially, we assessed the impact on mouse body weight after injecting live *E. coli* K1 (Bac (+)), inactivated *E. coli* K1 (Bac (–)), NAs-ΔBac (+), or NAs-ΔBac (–). As shown in Fig. 5(b), body weights significantly declined 5 days post-injection with either Bac (+) or Bac (–) at doses ≥ 1×10^6 CFU, indicating their extreme pathogenicity. In contrast, mice injected with NAs-ΔBac (–) at doses up to ~ 1×10^9 CFU survived for 14 days post-injection, although their body weights were somewhat reduced at higher doses. Consequently, we selected a moderate dose of ~ 1×10^7 CFU of NAs-ΔBac (–) per mouse for subsequent tests. We then cultured homogenates of primary organs on LB agar plates to evaluate bacterial growth in the organs. 12 h post-injection, NAs-ΔBac (+) was detected in the brain and increased over time (Fig. 5(c)), while its presence in other organs, such as the liver, declined. In contrast, nearly no live bacteria were detected in any organs of the NAs-ΔBac (–) group (Fig. 5(d)).

We also conducted whole blood and serum biochemical analyses on mice treated with the tested dose of NAs-ΔBac (–). As expected, plasma levels of aspartate transaminase (AST) (Fig. 5(e)) and alanine transaminase (ALT) (Fig. 5(f)) increased following intravenous administration of NAs-Bac (–) after 72 h. However, these levels did not rise after NAs-ΔBac (–) injection, indicating no induction of acute hepatotoxicity or nephrotoxicity. Additionally, mice treated with NAs-Bac (–) exhibited significant increases in white blood cell (WBC) (Fig. 5(g)) and platelet (PLT) counts (Fig. 5(h)). 72 h post-injection of NAs-ΔBac (–), all serum biochemical markers and most routine blood data remained within normal limits compared to untreated healthy mice (Fig. S17 in the ESM). Finally, no significant histopathological abnormalities were observed in the hematoxylin and eosin (H&E)-stained major organs from healthy mice 30 days post-treatment (Fig. S18 in the ESM). Collectively, these results demonstrate the good

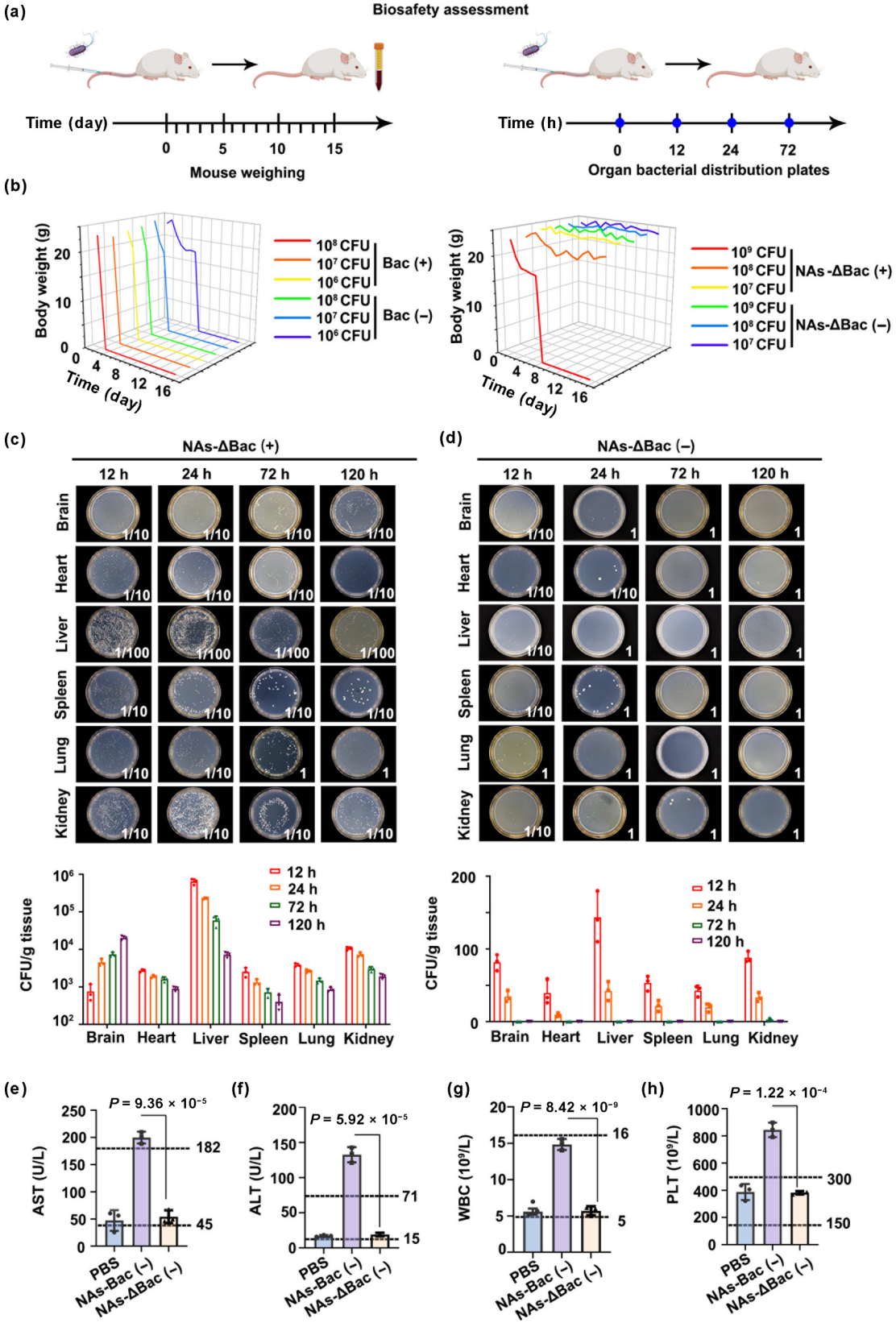

Figure 5 Biosafety assessment of the inactivated nanobacteria system. (a) Scheme illustrating the assessment of the biosafety of the constructed NAs-ΔBac (–) construct after intravenous injection into healthy mice. (b) Effects of the injected dose of NAs-Bac (+), NAs-Bac (–), NAs-ΔBac (+) or NAs-ΔBac (–) on the body weight of the mice. Homogenates of major organs of healthy mice after intravenous injection of (c) NAs-ΔBac (+) or (d) NAs-ΔBac (–) at a dose of ~ 1×10^7 CFU over time cultured on solid LB agar plates and corresponding quantification of bacterial counts. The levels of (e) AST, (f) ALT, (g) WBCs and (h) PLTs in healthy mice intravenously injected with NAs-Bac (–) or NAs-ΔBac (–) at a dose of 1.0×10^7 CFU per mouse for 72 h. All error bars represent the standard deviation determined from three independent assays. Statistical significance was calculated via one-way analysis of variance (ANOVA) with a Tukey post hoc test.

biocompatibility of the inactivated nanobacteria system.

3.6 *In vivo* evaluation of the antitumor ability of the inactivated nanobacteria system

Having established that inactivated nanobacteria can traverse the BBB, we evaluated its photothermal immune efficacy in orthotopic GBM-bearing mice, with a focus on selective glioma targeting. An orthotopic tumor model was generated by inoculating approximately 5×10^5 Gl261-Luc cells per animal *in situ* on day -7 (Fig. 6(a)). Once the GBM model was established, mice received intravenous treatments on days 0 (Treatment 1), 5 (Treatment 2), and 10 (Treatment 3). Photothermal treatment (PTT) was

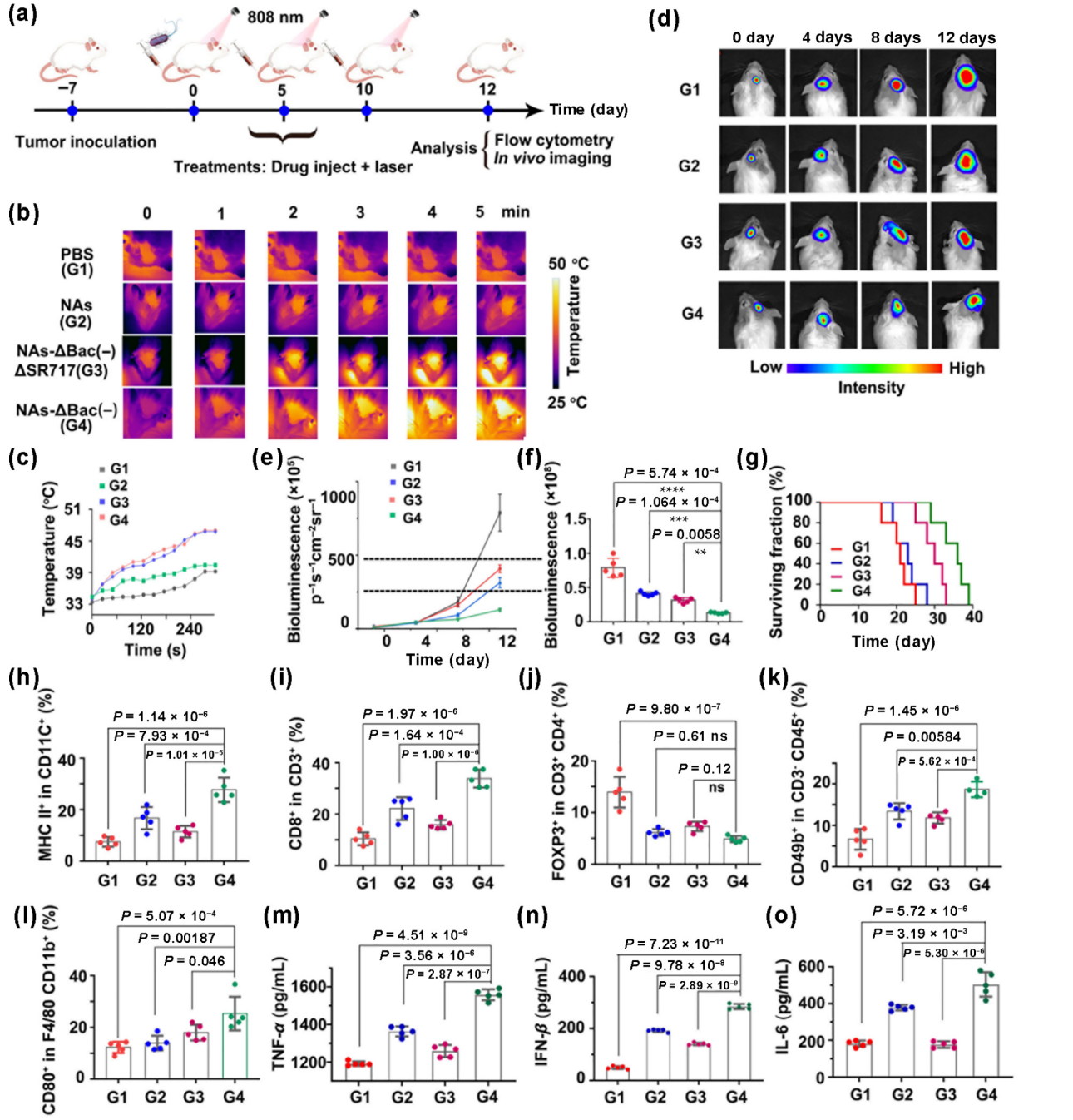

Figure 6 *In vivo* evaluation of the antitumor ability of the inactivated nanobacteria system. (a) A scheme illustrating NAs-ΔBac (−) therapy in a GBM-bearing mouse model. (b) Representative infrared images of the brains of GBM-bearing mice treated with PBS (G1), NAs (G2), NAs-ΔBac (−) ΔSR717 (*i.e.*, NAs-ΔBac (−) without SR717) (G3) or NAs-ΔBac (−) (G4) under 808 nm laser irradiation and (c) the corresponding temperature changes in the brain. (d) Representative *in vivo* bioluminescence images of GBM-bearing mice, (e) individual bioluminescence change curves and (f) semiquantification of bioluminescence intensity in the brain of GBM-bearing mice treated with PBS (G1), NAs (G2), NAs-ΔBac (−) ΔSR717 (G3) or NAs-ΔBac (−) (G4) under 808 nm laser irradiation. (g) Kaplan–Meier survival curves. Flow cytometric analysis of (h) mature DCs ($CD11c^+$ $MHC\ II^+$), (i) $CD8^+$ T cells ($CD3^+$ $CD8^+$), (j) Treg cells ($CD3^+$ $CD4^+$ $FOXP3^+$), (k) NK cells ($CD3^-$ $CD45^+$ $CD49b^+$) and (l) M1-type cells ($CD11b^+$ $F4/80^+$ $CD80^+$) in GBM-bearing mice after different treatments as indicated. Quantification of (m) TNF-α, (n) IFN-β and (o) IL-6 in the serum of GBM-bearing mice after different treatments as indicated. All imaging experiments were repeated three times with similar results. All error bars represent the standard deviation determined from five independent assays. Statistical significance was calculated via one-way analysis of variance (ANOVA) with a Tukey post hoc test.

administered under 808-nm laser irradiation, which was precisely focused on the tumor site. Laser irradiation was applied for 5 min, 8 h following each drug injection, ensuring targeted heating. To minimize potential damage to adjacent healthy brain tissue, temperature modulation was carefully controlled, focusing on achieving therapeutic efficacy against glioma cells without extending thermal effects beyond the tumor area. Mice were euthanized three days after Treatment 3, and tumors were harvested and homogenized for flow cytometric analysis [37, 63]. Cytokine concentrations in the tumor lysate supernatants were measured using ELISA kits as per the vendors' instructions. 8 h after NAs-ΔBac (–) injection, the mouse brains were irradiated with 808 nm light (1.2 W/cm^2, 5 min). Infrared camera images (Fig. 6(b)) showed a rapid temperature increase in the GBM tissue exclusively in the NAs-ΔBac (–) without SR717 and NAs-ΔBac (–) groups. Specifically, after 5 min of irradiation, the GBM surface temperature in the NAs-ΔBac (–) group reached 48 °C (Fig. 6(c)). No significant heating was observed in the other groups under the same conditions. Subsequent intravenous injections of NAs, NAs-ΔBac (–) without SR717, and NAs-ΔBac (–) were administered on days 5 and 10 post-initial injection. The anticancer effect was visualized every four days using bioluminescence imaging. Figures 6(d) and 6(e) show significantly dimmer bioluminescence signals of Gl261-Luc cells in the NAs-ΔBac (–) group compared to other groups. Quantitative analysis revealed that the NAs-ΔBac (–) system significantly inhibited tumor growth, achieving an inhibition rate of 83.5%, compared to 48.2% for NAs and 60.2% for NAs-ΔBac (–) without SR717 (Fig. 6(f)). Survival analysis indicated that mice in the NAs-ΔBac (–) group survived substantially longer than those in other groups (Fig. 6(g)).

To assess whether the NAs-ΔBac (–) system induces both adaptive and innate antitumor immunity, we performed flow cytometry analysis on various immune cell populations. We first evaluated the degree of DC maturation (CD11c$^+$ MHCII$^+$). The highest proportion of mature DCs was observed in the NAs-ΔBac (–) + laser group (27.7%), compared to 11.4% in the NAs-ΔBac (–) without SR717 + laser group, 16.7% in the NAs + laser group, and 7.47% in the PBS + laser group (Fig. 6(h) and Fig. S19 in the ESM). Next, we assessed the populations of cytotoxic T lymphocytes (CTLs) (CD3$^+$ CD8$^+$). The NAs-ΔBac (–) + laser group showed a 3.24-fold increase in CD8$^+$ T cells compared to the PBS + laser group (Fig. 6(i) and Fig. S20 in the ESM). Additionally, we evaluated regulatory T cells (Tregs) (CD3$^+$ CD4$^+$ Foxp3$^+$). The NAs-ΔBac (–) + laser group showed a 65.1% reduction in Treg populations compared to the PBS + laser group (Fig. 6(j) and Fig. S21 in the ESM). We also investigated innate antitumor immunity. The intratumoral frequencies of NK cells (CD3$^-$ CD45$^+$ CD49b$^+$) were significantly higher in the NAs-ΔBac (–) + laser group (2.85-fold increase) compared to the PBS + laser group (Fig. 6(k) and Fig. S22 in the ESM). M1 macrophage polarization (CD11b$^+$ F4/80$^+$ CD80$^+$) was also more pronounced in the NAs-ΔBac (–) + laser group (25.4%) compared to the PBS + laser group (12.3%) (Fig. 6(l) and Fig. S23 in the ESM). Finally, we measured levels of proinflammatory cytokines, including IFN-β, IL-6, and TNF-α, in serum samples from mice subjected to various treatments. The levels of these cytokines were highest in the NAs-ΔBac (–) + laser group (Figs. 6(m)–6(o)). These results collectively demonstrate that the STING-mediated bacterial delivery system can induce both adaptive and innate antitumor immunity, working synergistically to suppress GBM growth.

4 Conclusions

GBM treatment is challenged by the inability of therapeutic agents to cross the BBB. Here, we successfully developed a novel inactivated nanobacteria system. By knocking out the *msbB* gene, we reduced the pathogenicity of EC-K1. By further irradiating the bacterial cells with UV light, we eliminated their proliferation ability. The loaded therapeutics were made of GP, ICG and SR717-modified silica nanoparticles, which could be robustly internalized into attenuated EC-K1 through a bacteria-specific ABC sugar transporter pathway. These bacteria retain their chemotactic properties but lose pathogenicity, enabling safe intravenous administration. Upon laser irradiation, the bacteria release STING agonists, triggering a robust antitumor immune response. This approach significantly reduces tumor growth in mice, suggesting a promising new direction for GBM immunotherapy.

Electronic Supplementary Material: Supplementary material (further details of PCR results, CLSM images, flow cytometry analysis, blood biochemistry and hematology data and Sanger sequencing data) is available in the online version of this article at https://doi.org/10.26599/NR.2025.94907077.

Data availability

All data needed to support the conclusions in the paper are presented in the manuscript and the Electronic Supplementary Material. Additional data related to this paper may be requested from the corresponding author upon request.

Acknowledgements

We thank Prof. Liangzhu Feng (Soochow University, China) for his general help and valuable suggestions. Yao He discloses support for the research described in this study from the National Key R&D Program of China (No. 2023YFB3208200), the National Natural Science Foundation of China (Nos. 22393932, T2321005, and 21825402), the Science and Technology Development Fund, Macau SAR (Nos. 0002/2022/AKP and 0115/2023/RIA2), and the Program for Jiangsu Specially Ap-pointed Professors to Professor Yao He, a project funded by the Priority Academic Program Development of Jiangsu Higher Education Institutions (PAPD), 111 Project and Collaborative Innovation Center of Suzhou Nano Science and Technology (NANO-CIC). Houyu Wang provided support for the research de-scribed in this study from the National Natural Science Foundation of China (No. 22074101). Bin Song provided support for the research described in this study from the National Natural Science Foundation of China (No. 22204116) and the Natural Science Foundation of Jiangsu Province of China (No. BK20200851). Binbin Chu provided support for the research described in this study from the National Natural Science Foundation of China (No. 22204117).

Declaration of competing interest

All the contributing authors report no conflict of interests in this work.

Author contribution statement

C. J.: Data curation, project administration, validation, writing manuscript, experimental design. Y. P. J.: Data curation, project

administration, validation, experimental design. H. Y. X.: Project administration, writing manuscript. B. S.: Project administration, funding acquisition. B. B. C.: Project administration, funding acquisition. Y. H.: Project administration, funding acquisition. H. Y. W.: Project administration, funding acquisition, writing manuscript. All the authors have approved the final manuscript.

Informed consent

Not applicable.

Ethics statement

The animal experiments were carried out following the guidelines of Soochow University for the Care and Use of Laboratory Animals and were approved by the Committee on Ethical Use of Animals of Soochow University (Ethical code: SYXK(SU) 2021-0073).

Use of AI statement

None.

References

[1] Purow, B.; Schiff, D. Advances in the genetics of glioblastoma: Are we reaching critical mass. *Nat. Rev. Neurol.* **2009**, *5*, 419–426.

[2] GBD 2016 Brain and Other CNS Cancer Collaborators. Global, regional, and national burden of brain and other CNS cancer, 1990-2016: A systematic analysis for the Global Burden of Disease Study 2016. *Lancet Neurol.* **2019**, *18*, 376–393.

[3] Song, E.; Mao, T. Y.; Dong, H. P.; Boisserand, L. S. B.; Antila, S.; Bosenberg, M.; Alitalo, K.; Thomas, J. L.; Iwasaki, A. VEGF-C-driven lymphatic drainage enables immunosurveillance of brain tumours. *Nature* **2020**, *577*, 689–694.

[4] Galon, J.; Bruni, D. Approaches to treat immune hot, altered and cold tumours with combination immunotherapies. *Nat. Rev. Drug Discov.* **2019**, *18*, 197–218.

[5] Mullard, A. Can innate immune system targets turn up the heat on 'cold' tumours. *Nat. Rev. Drug Discov.* **2018**, *17*, 3–5.

[6] van den Bent, M. J.; Geurts, M.; French, P. J.; Smits, M.; Capper, D.; Bromberg, J. E. C.; Chang, S. M. Primary brain tumours in adults. *Lancet* **2023**, *402*, 1564–1579.

[7] Sattiraju, A.; Kang, S.; Giotti, B.; Chen, Z. H.; Marallano, V. J.; Brusco, C.; Ramakrishnan, A.; Shen, L.; Tsankov, A. M.; Hambardzumyan, D. et al. Hypoxic niches attract and sequester tumor-associated macrophages and cytotoxic T cells and reprogram them for immunosuppression. *Immunity* **2023**, *56*, 1825–1843.e6.

[8] Samson, N.; Ablasser, A. The cGAS-STING pathway and cancer. *Nat. Cancer* **2022**, *3*, 1452–1463.

[9] Li, X. F.; Khorsandi, S.; Wang, Y. F.; Santelli, J.; Huntoon, K.; Nguyen, N.; Yang, M. M.; Lee, D.; Lu, Y. F.; Gao, R. Q. et al. Cancer immunotherapy based on image-guided STING activation by nucleotide nanocomplex-decorated ultrasound microbubbles. *Nat. Nanotechnol.* **2022**, *17*, 891–899.

[10] Sun, X. Q.; Zhang, Y.; Li, J. Q.; Park, K. S.; Han, K.; Zhou, X. W.; Xu, Y.; Nam, J.; Xu, J.; Shi, X. Y. et al. Amplifying STING activation by cyclic dinucleotide-manganese particles for local and systemic cancer metalloimmunotherapy. *Nat. Nanotechnol.* **2021**, *16*, 1260–1270.

[11] Dane, E. L.; Belessiotis-Richards, A.; Backlund, C.; Wang, J. N.; Hidaka, K.; Milling, L. E.; Bhagchandani, S.; Melo, M. B.; Wu, S. W.; Li, N. et al. STING agonist delivery by tumour-penetrating PEG-lipid nanodiscs primes robust anticancer immunity. *Nat. Mater.* **2022**, *21*, 710–720.

[12] Li, S. X.; Luo, M.; Wang, Z. H.; Feng, Q.; Wilhelm, J.; Wang, X.; Li, W.; Wang, J.; Cholka, A.; Fu, Y. X. et al. Prolonged activation of innate immune pathways by a polyvalent STING agonist. *Nat. Biomed. Eng.* **2021**, *5*, 455–466.

[13] Wang, F. H.; Su, H.; Xu, D. Q.; Dai, W. B.; Zhang, W. J.; Wang, Z. Y.; Anderson, C. F.; Zheng, M. Z.; Oh, R.; Wan, F. Y. et al. Tumour sensitization via the extended intratumoural release of a STING agonist and camptothecin from a self-assembled hydrogel. *Nat. Biomed. Eng.* **2020**, *4*, 1090–1101.

[14] Shae, D.; Becker, K. W.; Christov, P.; Yun, D. S.; Lytton-Jean, A. K. R.; Sevimli, S.; Ascano, M.; Kelley, M.; Johnson, D. B.; Balko, J. M. et al. Endosomolytic polymersomes increase the activity of cyclic dinucleotide STING agonists to enhance cancer immunotherapy. *Nat. Nanotechnol.* **2019**, *14*, 269–278.

[15] Leventhal, D. S.; Sokolovska, A.; Li, N.; Plescia, C.; Kolodziej, S. A.; Gallant, C. W.; Christmas, R.; Gao, J. R.; James, M. J.; Abin-Fuentes, A. et al. Immunotherapy with engineered bacteria by targeting the STING pathway for anti-tumor immunity. *Nat. Commun.* **2020**, *11*, 2379.

[16] Garland, K. M.; Sheehy, T. L.; Wilson, J. T. Chemical and biomolecular strategies for STING pathway activation in cancer immunotherapy. *Chem. Rev.* **2022**, *122*, 5977–6039.

[17] Sun, X. Q.; Huang, X. H.; Park, K. S.; Zhou, X. W.; Kennedy, A. A.; Pretto, C. D.; Wu, Q.; Wan, Z. Y.; Xu, Y.; Gong, W. et al. Self-assembled STING-activating coordination nanoparticles for cancer immunotherapy and vaccine applications. *ACS Nano* **2024**, *18*, 10439–10453.

[18] Xu, L.; Deng, H. P.; Wu, L.; Wang, D. L.; Shi, L. L.; Qian, Q. H.; Huang, X. G.; Zhu, L. J.; Gao, X. H.; Yang, J. P. et al. Supramolecular cyclic dinucleotide nanoparticles for STING-mediated cancer immunotherapy. *ACS Nano* **2023**, *17*, 10090–10103.

[19] Li, Q. G.; Dong, Z. L.; Cao, Z. Q.; Lei, H. L.; Wang, C. J.; Hao, Y.; Feng, L. Z.; Liu, Z. A general biomineralization strategy to synthesize autologous cancer vaccines with cGAS-STING activating capacity for postsurgical immunotherapy. *ACS Nano* **2023**, *17*, 10496–10510.

[20] Yang, H.; Yang, S. S.; Guo, Q. S.; Sheng, J. F.; Mao, Z. W. ATP-responsive manganese-based bacterial materials synergistically activate the cGAS-STING pathway for tumor immunotherapy. *Adv. Mater.* **2024**, *36*, 2310189.

[21] Wu, J. X.; Sun, L. J.; Chen, X.; Du, F. H.; Shi, H. P.; Chen, C.; Chen, Z. J. Cyclic GMP-AMP is an endogenous second messenger in innate immune signaling by cytosolic DNA. *Science* **2013**, *339*, 826–830.

[22] Ishikawa, H.; Ma, Z.; Barber, G. N. STING regulates intracellular DNA-mediated, type I interferon-dependent innate immunity. *Nature* **2009**, *461*, 788–792.

[23] Sun, L. J.; Wu, J. X.; Du, F. H.; Chen, X.; Chen, Z. J. Cyclic GMP-AMP synthase is a cytosolic DNA sensor that activates the type I interferon pathway. *Science* **2013**, *339*, 786–791.

[24] Corrales, L.; Glickman, L. H.; McWhirter, S. M.; Kanne, D. B.; Sivick, K. E.; Katibah, G. E.; Woo, S. R.; Lemmens, E.; Banda, T.; Leong, J. J. et al. Direct activation of STING in the tumor microenvironment leads to potent and systemic tumor regression and immunity. *Cell Rep.* **2015**, *11*, 1018–1030.

[25] Demaria, O.; De Gassart, A.; Coso, S.; Gestermann, N.; Di Domizio, J.; Flatz, L.; Gaide, O.; Michielin, O.; Hwu, P.; Petrova, T. V. et al. STING activation of tumor endothelial cells initiates spontaneous and therapeutic antitumor immunity. *Proc. Natl. Acad. Sci. USA* **2015**, *112*, 15408–15413.

[26] Zhou, S. B.; Gravekamp, C.; Bermudes, D.; Liu, K. Tumour-targeting bacteria engineered to fight cancer. *Nat. Rev. Cancer* **2018**, *18*, 727–743.

[27] Dang, L. H.; Bettegowda, C.; Huso, D. L.; Kinzler, K. W.; Vogelstein, B. Combination bacteriolytic therapy for the treatment of experimental tumors. *Proc. Natl. Acad. Sci. USA* **2001**, *98*, 15155–15160.

[28] Hosseinidoust, Z.; Mostaghaci, B.; Yasa, O.; Park, B. W.; Singh, A. V.; Sitti, M. Bioengineered and biohybrid bacteria-based systems for drug delivery. *Adv. Drug Deliv.* **2016**, *106*, 27–44.

[29] Forbes, N. S. Engineering the perfect (bacterial) cancer therapy. *Nat.*

Rev. Cancer **2010**, *10*, 785–794.
[30] Liu, Y.; Zhang, M. M.; Wang, X. Y.; Yang, F. M.; Cao, Z. P.; Wang, L.; Liu, J. Y. Dressing bacteria with a hybrid immunoactive nanosurface to elicit dual anticancer and antiviral immunity. *Adv. Mater.* **2023**, *35*, 2210949.
[31] Jiang, J. W.; Huang, Y. J.; Zeng, Z. S.; Zhao, C. S. Harnessing engineered immune cells and bacteria as drug carriers for cancer immunotherapy. *ACS Nano* **2023**, *17*, 843–884.
[32] Chen, W. F.; Wang, Y.; Qin, M.; Zhang, X. D.; Zhang, Z. R.; Sun, X.; Gu, Z. Bacteria-driven hypoxia targeting for combined biotherapy and photothermal therapy. *ACS Nano* **2018**, *12*, 5995–6005.
[33] Han, D. D.; Wang, F.; Ma, Y. C.; Zhao, Y.; Zhang, W.; Zhang, Z. Y.; Liu, H. F.; Yang, X. J.; Zhang, C.; Zhang, J. C. et al. Redirecting antigens by engineered photosynthetic bacteria and derived outer membrane vesicles for enhanced cancer immunotherapy. *ACS Nano* **2023**, *17*, 18716–18731.
[34] Liu, X. M.; Sun, M. Y.; Pu, F.; Ren, J. S.; Qu, X. G. Transforming intratumor bacteria into immunopotentiators to reverse cold tumors for enhanced immuno-chemodynamic therapy of triple-negative breast cancer. *J. Am. Chem. Soc.* **2023**, *145*, 26296–26307.
[35] Liu, K. K.; Wang, L. N.; Peng, J.; Lyu, Y. J.; Li, Y. M.; Duan, D. Y.; Zhang, W. Y.; Wei, G. J.; Li, T. P.; Niu, Y. J. et al. Drug-loaded Bacillus Calmette-Guérin bacteria for immuno-chemo combo therapy in bladder cancer. *Adv. Mater.* **2024**, *36*, 2310735.
[36] Pan, P.; Dong, X.; Chen, Y.; Zeng, X.; Zhang, X. Z. Engineered bacteria for enhanced radiotherapy against breast carcinoma. *ACS Nano* **2022**, *16*, 801–812.
[37] Sun, R.; Liu, M. Z.; Lu, J. P.; Chu, B. B.; Yang, Y. M.; Song, B.; Wang, H. Y.; He, Y. Bacteria loaded with glucose polymer and photosensitive ICG silicon-nanoparticles for glioblastoma photothermal immunotherapy. *Nat. Commun.* **2022**, *13*, 5127.
[38] Pinho-Ribeiro, F. A.; Deng, L. W.; Neel, D. V.; Erdogan, O.; Basu, H.; Yang, D. P.; Choi, S.; Walker, A. J.; Carneiro-Nascimento, S.; He, K. et al. Bacteria hijack a meningeal neuroimmune axis to facilitate brain invasion. *Nature* **2023**, *615*, 472–481.
[39] Kim, K. S. Mechanisms of microbial traversal of the blood-brain barrier. *Nat. Rev. Microbiol.* **2008**, *6*, 625–634.
[40] Coureuil, M.; Lécuyer, H.; Bourdoulous, S.; Nassif, X. A journey into the brain: Insight into how bacterial pathogens cross blood-brain barriers. *Nat. Rev. Microbiol.* **2017**, *15*, 149–159.
[41] Harimoto, T.; Hahn, J.; Chen, Y. Y.; Im, J.; Zhang, J.; Hou, N.; Li, F. D.; Coker, C.; Gray, K.; Harr, N. et al. A programmable encapsulation system improves delivery of therapeutic bacteria in mice. *Nat. Biotechnol.* **2022**, *40*, 1259–1269.
[42] Ma, X. T.; Liang, X. L.; Li, Y.; Feng, Q. Q.; Cheng, K. M.; Ma, N. N.; Zhu, F.; Guo, X. J.; Yue, Y. L.; Liu, G. N. et al. Modular-designed engineered bacteria for precision tumor immunotherapy via spatiotemporal manipulation by magnetic field. *Nat. Commun.* **2023**, *14*, 1606.
[43] Chen, Q. W.; Qiao, J. Y.; Liu, X. H.; Zhang, C.; Zhang, X. Z. Customized materials-assisted microorganisms in tumor therapeutics. *Chem. Soc. Rev.* **2021**, *50*, 12576–12615.
[44] Geng, Z. M.; Cao, Z. P.; Liu, R.; Liu, K.; Liu, J. Y.; Tan, W. H. Aptamer-assisted tumor localization of bacteria for enhanced biotherapy. *Nat. Commun.* **2021**, *12*, 6584.
[45] Park, B. W.; Zhuang, J.; Yasa, O.; Sitti, M. Multifunctional bacteria-driven microswimmers for targeted active drug delivery. *ACS Nano* **2017**, *11*, 8910–8923.
[46] Li, J. J.; Xia, Q.; Guo, H. Y.; Fu, Z. Z.; Liu, Y.; Lin, S. S.; Liu, J. Y. Decorating bacteria with triple immune nanoactivators generates tumor-resident living immunotherapeutics. *Angew. Chem., Int. Ed.* **2022**, *61*, e202202409.
[47] Wang, L.; Cao, Z. P.; Zhang, M. M.; Lin, S. S.; Liu, J. Y. Spatiotemporally controllable distribution of combination therapeutics in solid tumors by dually modified bacteria. *Adv. Mater.* **2022**, *34*, 2106669.
[48] Yan, X. H.; Zhou, Q.; Vincent, M.; Deng, Y.; Yu, J. F.; Xu, J. B.; Xu, T. T.; Tang, T.; Bian, L. M.; Wang, Y. X. J. et al. Multifunctional biohybrid magnetite microrobots for imaging-guided therapy. *Sci. Rob.* **2017**, *2*, eaaq1155.
[49] Cao, Z. P.; Wang, X. Y.; Pang, Y.; Cheng, S. S.; Liu, J. Y. Biointerfacial self-assembly generates lipid membrane coated bacteria for enhanced oral delivery and treatment. *Nat. Commun.* **2019**, *10*, 5783.
[50] Tang, J. L.; Chu, B. B.; Wang, J. H.; Song, B.; Su, Y. Y.; Wang, H. Y.; He, Y. Multifunctional nanoagents for ultrasensitive imaging and photoactive killing of Gram-negative and Gram-positive bacteria. *Nat. Commun.* **2019**, *10*, 4057.
[51] Yang, Y. M.; Chu, B. B.; Cheng, J. Y.; Tang, J. L.; Song, B.; Wang, H. Y.; He, Y. Bacteria eat nanoprobes for aggregation-enhanced imaging and killing diverse microorganisms. *Nat. Commun.* **2022**, *13*, 1255.
[52] Liu, M. Z.; Chu, B. B.; Sun, R.; Ding, J. L.; Ye, H.; Yang, Y. M.; Wu, Y. Q.; Shi, H. L.; Song, B.; He, Y. et al. Antisense oligonucleotides selectively enter human-derived antibiotic-resistant bacteria through bacterial-specific ATP-binding cassette sugar transporter. *Adv. Mater.* **2023**, *35*, 2300477.
[53] Zhang, Q.; Song, B.; Xu, Y. N.; Yang, Y. M.; Ji, J.; Cao, W. J.; Lu, J. P.; Ding, J. L.; Cao, H. T.; Chu, B. B. et al. *In vivo* bioluminescence imaging of natural bacteria within deep tissues via ATP-binding cassette sugar transporter. *Nat. Commun.* **2023**, *14*, 2331.
[54] Chin, E. N.; Yu, C. G.; Vartabedian, V. F.; Jia, Y.; Kumar, M.; Gamo, A. M.; Vernier, W.; Ali, S. H.; Kissai, M.; Lazar, D. C. et al. Antitumor activity of a systemic STING-activating non-nucleotide cGAMP mimetic. *Science* **2020**, *369*, 993–999.
[55] Janjua, T. I.; Cao, Y. X.; Yu, C. Z.; Popat, A. Clinical translation of silica nanoparticles. *Nat. Rev. Mater.* **2021**, *6*, 1072–1074.
[56] Yang, Y. N.; Zhang, M.; Song, H.; Yu, C. Z. Silica-based nanoparticles for biomedical applications: From nanocarriers to biomodulators. *Acc. Chem. Res.* **2020**, *53*, 1545–1556.
[57] Zlitni, A.; Gowrishankar, G.; Steinberg, I.; Haywood, T.; Gambhir, S. S. Maltotriose-based probes for fluorescence and photoacoustic imaging of bacterial infections. *Nat. Commun.* **2020**, *11*, 1250.
[58] Ning, X. H.; Seo, W.; Lee, S.; Takemiya, K.; Rafi, M.; Feng, X. L.; Weiss, D.; Wang, X. J.; Williams, L.; Camp, V. M. et al. PET imaging of bacterial infections with fluorine-18-labeled maltohexaose. *Angew. Chem., Int. Ed.* **2014**, *53*, 14096–14101.
[59] Ning, X. H.; Lee, S.; Wang, Z. R.; Kim, D.; Stubblefield, B.; Gilbert, E.; Murthy, N. Maltodextrin-based imaging probes detect bacteria *in vivo* with high sensitivity and specificity. *Nat. Mater.* **2011**, *10*, 602–607.
[60] Koebnik, R. Structural and functional roles of the surface-exposed loops of the β-barrel membrane protein OmpA from *Escherichia coli*. *J. Bacteriol.* **1999**, *181*, 3688–3694.
[61] Khan, N. A.; Shin, S.; Chung, J. W.; Kim, K. J.; Elliott, S.; Wang, Y.; Kim, K. S. Outer membrane protein A and cytotoxic necrotizing factor-1 use diverse signaling mechanisms for *Escherichia coli* K1 invasion of human brain microvascular endothelial cells. *Microb. Pathog.* **2003**, *35*, 35–42.
[62] Mittal, R.; Prasadarao, N. V. gp96 expression in neutrophils is critical for the onset of Escherichia coli K1 (RS218) meningitis. *Nat. Commun.* **2011**, *2*, 552
[63] Lu, J. P.; Ding, J. L.; Chu, B. B.; Ji, C.; Zhang, Q.; Xu, Y. N.; Song, B.; Wang, H. Y.; He, Y. Inactive Trojan bacteria as safe drug delivery vehicles crossing the blood-brain barrier. *Nano Lett.* **2023**, *23*, 4326–4333.